Lead-free flexible perovskite solar cells with interfacial native oxide have >10% efficiency, and simultaneously enhanced stability and reliability

Min Chen,^{1,2,†,*} Qingshun Dong,^{3,†} Chuanxiao Xiao,^{2,†} Xiaopeng Zheng,² Zhenghong Dai,¹ Yantao Shi,³ Joseph M. Luther,² Nitin P. Padture ^{1,*}

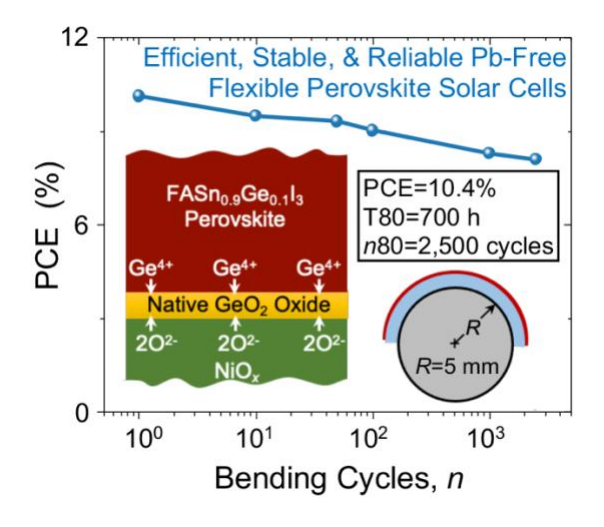
- School of Engineering, Brown University, Providence, Rhode Island, 02912, United States
 National Renewable Energy Laboratory, Golden, CO, 80401, United States
- ³ State Key Laboratory of Fine Chemicals, Department of Chemistry, School of Chemical Engineering, Dalian University of Technology, Dalian, 116024, China

† These authors contributed equally

ABSTRACT

Here we demonstrate an innovative compositional and interfacial engineering approach to achieve Pb-free flexible perovskite solar cells (f-PSCs) with an unprecedented combination of the highest efficiency reported to-date (10.43%), together with enhanced operational stability and mechanical reliability. The key to this approach is alloying of FASnI₃ metal halide perovskite (MHP) thin film with Ge²⁺ to stabilize the Sn²⁺ oxidation state in the MHP, together with the use of a NiO_x hole transport layer. We show that this results in the *in situ* formation of a thin amorphous GeO₂ native oxide layer at the NiO_x/FASn_{0.9}Ge_{0.1}I₃ interface. This layer not only passivates that critical interface but also enhances the interfacial mechanical bonding.

GRAPHICAL ABSTRACT



^{*} Emails: min_chen1@alumni.brown.edu (M.C.) and nitin_padture@brown.edu (N.P.P.)

Since the first report by Miyasaka and co-workers in 2009,¹ there has been extensive research into the use of metal halide perovskites (MHPs) as light-absorbers in potentially low-cost solar cells.² As a result, the record certified power conversion efficiency (PCE) of perovskite solar cells (PSCs) now stands at 25.7%,³ rivaling traditional silicon-based solar cells. PSCs have an unique advantage over other established commercial PV technologies in that they can be deposited on thin plastic substrates which makes them highly flexible and lightweight.⁴⁻⁷ Unfortunately, the MHPs used in state-of-the-art rigid and flexible PSCs (f-PSCs) contain toxic lead (Pb), which could present a hurdle in the path towards their commercialization.^{8, 9} While risk of possible Pb contamination in the case of tightly-controlled utility-scale solar farms can be managed effectively, that approach may not feasible in the case of f-PSCs that are expected to be used in consumer applications such as portable chargers, wearables, tents, backpacks, deployable rollups, cars, drones, sails, *etc*.⁴⁻⁷ Since many countries impose severe restrictions on Pb content in consumer devices, f-PSCs could attract greater market adoption if Pb-free alternatives could be developed.⁹

Significant amount of research efforts has been devoted to replacing Pb in PSCs with other lower toxicity elements, ¹⁰ including silver (Ag), ¹¹ bismuth (Bi), ¹² antimony (Sb), ¹³ titanium (Ti), ¹⁴, 15 germanium (Ge), 16 tin (Sn), 17, 18 and mixed Sn-Ge. 19 Among these candidates, Sn-based MHPs have shown the greatest promise, 18 with the highest reported PCE of 14.7% in rigid PSCs, 20 attempting to close the gap between Sn-based and Pb-based PSCs. However, in the case of Pb-free f-PSC, the highest reported PCE is quite a bit lower (8.46%).²¹ The lower PCE in Sn-based PSCs in general is attributed primarily to the intrinsic instability of the Sn²⁺ oxidation state in the MHP.²² The Sn-vacancies generated during the Sn²⁺ → Sn⁴⁺ oxidation cause metallic conductivity, ²³ and they also serve as nonradiative recombination centers for photocarriers, ²⁴ resulting in open-circuit voltage (V_{OC}) losses.²⁵ Several strategies have been proposed for retaining the Sn²⁺ oxidation state in Sn-based PSCs, which include the use of anti-oxidants in the precursors, 26-28 and defect passivation via incorporation of bulky organic cations.^{29,30} Previously we have shown that alloying Sn-based MHPs with Ge²⁺ as a substitutional solid solute can also result in the stabilization of Sn²⁺, together with the formation of a stable, protective native oxide. ¹⁹ Inspired by this strategy, Nishimura, et al. 31 demonstrated a PCE of over 13% in rigid PSCs incorporating GeI₂-doped Snbased MHP thin films. It is worth noting that, unlike Pb-based PSCs, the highest PCEs in Sn-based PSCs are obtained using the *p-i-n* (inverted) architecture. Inverted PSCs typically utilize an organic such poly(3,4-ethylenedioxythiophene) hole-transport layer (HTL), as polystyrene sulfonate (PEDOT:PSS) or polytriarylamine (PTAA), which limits their long-term operational

stability.³² A way around this problem is to use an inorganic HTL such as nickel oxide (NiO_x). Unfortunately, the Ni³⁺ within NiO_x can react with the Sn-based MHP thin film that is in contact, resulting in the Sn²⁺ \rightarrow Sn⁴⁺ oxidation. Also, in the case of f-PSCs in general, typically they are subjected to more severe externally applied mechanical stresses during manufacturing and service (bending, stretching, twisting) compared to their rigid PSC counterparts, which can result in the fracture of the brittle MHP thin film, the other functional layers, and/or the interfaces.⁷ Thus, enhancing the mechanical reliability of f-PSCs is particularly important.⁴⁻⁷

Here we report a new approach that addresses all of these issues in f-PSCs, and it entails Ge²⁺-alloying of the Pb-free formamidinium tin triiodide (HC(NH₂)₂SnI₃ or FASnI₃) MHP thin films. We show that this results in the *in situ* growth of a thin (~3 nm) amorphous native oxide (GeO₂) at the interface between the MHP thin film and the NiO_x HTL. The native oxide, which allows tunneling of holes while preventing the oxidation of the Sn-based MHP layer by blocking ionic diffusion, serves as a passivating layer. Also, it enhances the mechanical bonding of that critical interface. As a result, FASn_{0.9}Ge_{0.1}I₃-based f-PCSs show an unprecedented combination of performance metrics: highest PCE reported so far (10.43%, with reduced hysteresis), enhanced operational stability (700 h T80, time at 80% initial PCE retained) under continuous 1-sun illumination (maximum power-point (MPP) tracking, N₂ atmosphere), and enhanced mechanical reliability (2,500 cycles *n*80 bending durability, cycles (*n*) at 80% initial PCE retained) under tension-only bending at radius *R*=5 mm in N₂ atmosphere.

The popular Pb-free MHP, FASnI₃ with 5 mol% excess SnF₂, is chosen here, which has been optimized for high PCE and stability.³³ The Ge²⁺-alloyed MHP is of the composition FASn-0.9Ge_{0.1}I₃, also with 5 mol % excess SnF₂. This composition was chosen based on a preliminary optimization study (not presented here). For the initial characterization experiments, thin films (~300 nm) of these MHPs were deposited using the solvent-engineering method ³⁴ on NiO_x HTL on bare glass substrates, followed by annealing at 100 °C for 20 min. Figure 1A and 1D are top-surface scanning electron microscope (SEM) images of the FASnI₃ and the FASn_{0.9}Ge_{0.1}I₃ thin films, respectively, showing uniform coverage. The average grain sizes are estimated at ~250 nm and ~300 nm for the FASnI₃ and the FASn_{0.9}Ge_{0.1}I₃ thin films, respectively. The indexed X-ray diffraction (XRD) pattern of FASnI₃ in the FASn_{0.9}Ge_{0.1}I₃ thin films are presented in Figs. 1B and 1E, respectively. While the FASnI₃ thin film appears to be random polycrystalline, FASn_{0.9}Ge_{0.1}I₃ thin film shows some texture (100), which can be attributed to its relatively larger grain size.^{35, 36} The UV-*vis* spectra in Figs. 1C and 1F of the FASnI₃ and the FASn_{0.9}Ge_{0.1}I₃ thin films,

respectively, show comparable absorption, but the FASn_{0.9}Ge_{0.1}I₃ thin film has a slightly lower Urbach energy (98 meV) compared to that the FASn₁₃ thin film (135 meV). It should be noted that the photoluminescence (PL) intensity of the FASn_{0.9}Ge_{0.1}I₃ thin film (Fig. 1F) is significantly lower than that of the FASn₁₃ thin film (Fig. 1C), indicating much improved holes extraction at the interface with the NiO_x HTL. (The corresponding PL spectra of the MHP thin films deposited on bare glass substrates, without the NiO_x HTL, in Fig. S1 in the Supporting Information (SI) show much stronger PL signal from FASn_{0.9}Ge_{0.1}I₃ compared to FASn₁₃, attesting to the beneficial effect of Ge²⁺ alloying.) The PL peak (~885 nm) of the FASn_{0.9}Ge_{0.1}I₃ thin film is slightly blue-shifted compared to that of the of FASn₁₃ thin film (~897 nm) owing to the widening of the bandgap due to Ge²⁺ alloying.³⁷

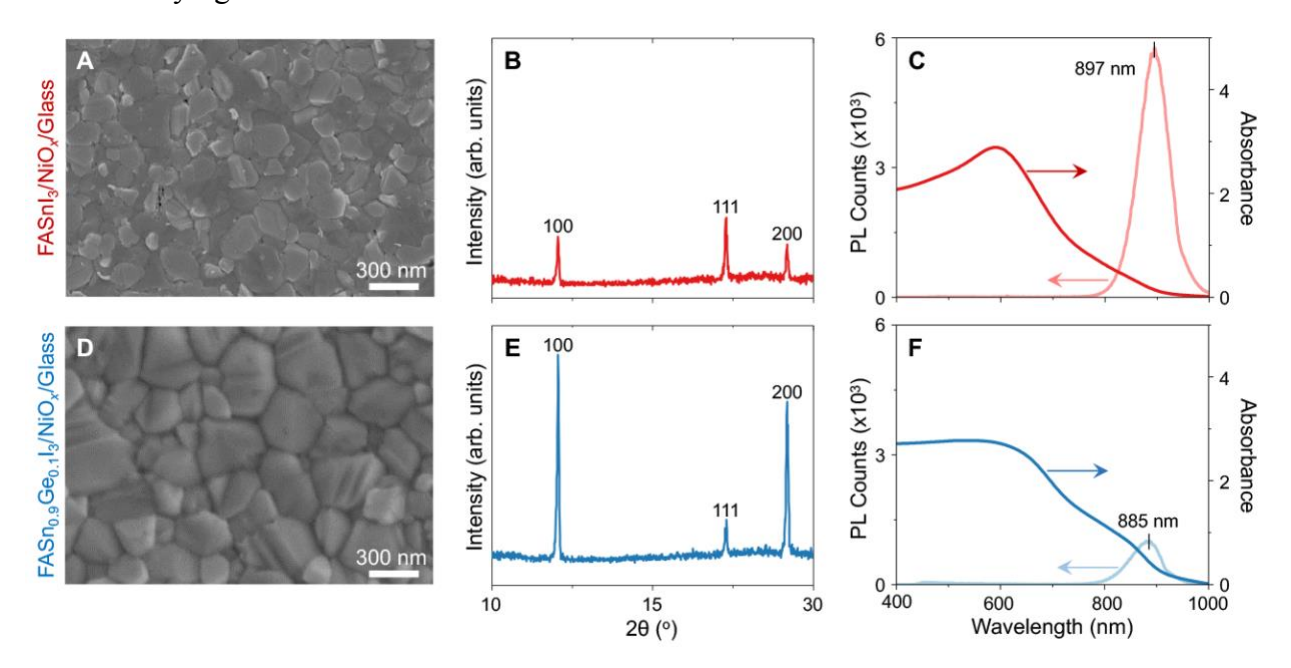


Figure 1. Characterization of the MHP thin films on NiO_x/glass substrates. Top-surface SEM images: (A) FASnI₃ and (D) FASn_{0.9}Ge_{0.1}I₃. Indexed XRD patterns: (B) FASnI₃ and (E) FASn_{0.9}Ge_{0.1}I₃. UV-vis absorption and PL spectra: (C) FASnI₃ and (F) FASn_{0.9}Ge_{0.1}I₃.

The FASnI₃ and the FASn_{0.9}Ge_{0.1}I₃ thin films on NiO_x/glass substrates were further characterized using X-ray photoelectron spectroscopy (XPS). A polymethyl methacrylate (PMMA) polymer layer was spin-coated on top to protect the thin film from degrading during the transfer of the samples. Here, XPS Ge 3*d* and Sn 3*d* core-level spectra were obtained at different sputtering depths. The basic scheme for depth-wise XPS is illustrated in Fig. 2A. The XPS Ge 3*d* spectra in Fig. 2B show that the surface and the middle part of the FASn_{0.9}Ge_{0.1}I₃ thin film contain

mostly Ge²⁺, with a slight amount of metallic Ge⁰ detected, which is inevitably generated due to the argon (Ar) sputtering. However, the bottom-interface between the FASn_{0.9}Ge_{0.1}I₃ thin film and NiO_x HTL is characterized by Ge⁴⁺-O²⁻ and Ge⁴⁺-I⁻ bonding peaks primarily. This indicates that the *in situ* grown interfacial native oxide, GeO₂, is chemically bonded with the MHP thin film (Ge⁴⁺-I⁻) and with the NiO_x HTL (Ge⁴⁺-O²⁻) on either side. (Note that the XPS spectra from independent standard samples, GeO₂ and GeI₄, as shown in Fig. S2 in the SI, were used to identify the Ge⁴⁺-O²⁻ and Ge⁴⁺-I⁻ bonding peaks.) The XPS Sn 3*d* spectra in Fig. 2C confirms Sn²⁺ valence state in the entire FASn_{0.9}Ge_{0.1}I₃ thin film as a result of the protection provided by the interfacial GeO₂ native oxide.

Transmission electron microscopy (TEM) of the interfacial GeO₂ native oxide was also performed. Here, cross-sectional TEM specimens were carefully prepared using focused ion beam (FIB), and were transferred to the TEM. Figure S3 in the SI is a high-angle annular dark-field (HAADF) TEM image of the cross-section, and the higher resolution inset shows a thin amorphous layer (~3 nm) sandwiched between the crystalline FASn_{0.9}Ge_{0.1}I₃ thin film and the NiO_x HTL. Since native oxides are typically amorphous, that layer is deemed to be the interfacial GeO₂ native oxide. Unfortunately, due to e-beam degradation in the TEM, energy dispersive spectroscopy (EDS) could not be performed reliably on that layer to characterize its chemistry. Therefore, timeof-flight secondary ion mass spectroscopy (TOF-SIMS) was performed as a function of depth. The results presented in Fig. S4A in the SI clearly show the Ge-rich interfacial layer. In addition, Ge elemental maps of top, middle, and bottom-interface confirm uniformly distributed abundance of Ge across the thin film (Fig. S4B-D in the SI). Further control XPS experiments were performed on both FASnI₃ thin film on NiO_x HTL and FASn_{0.9}Ge_{0.1}I₃ thin film on PEDOT:PSS HTL. In the case of the former, Fig. S5 in the SI shows significant amount of Sn⁴⁺ at the FASnI₃/NiO_x interface, which is the result of reaction with the Ni^{3+} in NiO_x . In the case of the latter, Ge^{4+} is not seen in Fig. S6 in the SI, confirming the key role played by NiO_x in the *in-situ* formation of the interfacial GeO₂ native oxide. Note that this native-oxide formation mechanism is similar to GeO₂-containing native oxides in other cases, but there the oxidation source is atmospheric oxygen. 19, 38

Considering all the results from XPS, TEM, and TOF-SIMS characterization, we conclude the desirable existence of an amorphous GeO_2 native oxide of ~3 nm thickness that has formed *in situ* at the interface between the $FASn_{0.9}Ge_{0.1}I_3$ thin film and the NiO_x HTL. The genesis of this unique GeO_2 native oxide in this system is attributed to the preferential reaction between the Ge^{2+} in the $FASn_{0.9}Ge_{0.1}I_3$ thin film and the Ni^{3+} present in the NiO_x HTL.

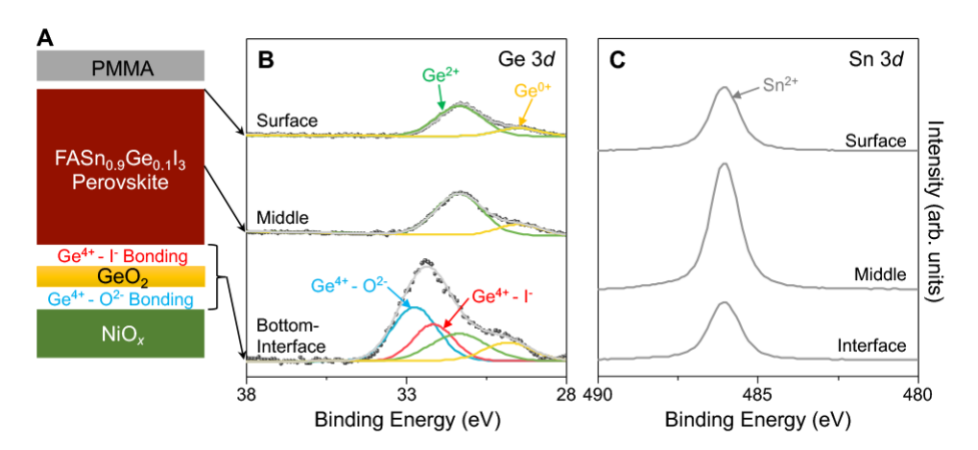


Figure 2. XPS characterization $FASn_{0.9}Ge_{0.1}I_3$ thin films on $NiO_x/glass$ substrates. (A) Schematic illustration (exploded view) of the depth-wise XPS characterization (not to scale). Fitted and deconvoluted XPS spectra at different sputtered depths: (B) Ge 3*d* and (C) Sn 3*d*.

The FASnI₃ and the FASn_{0.9}Ge_{0.1}I₃ thin films (~300 nm thickness) were incorporated into f-PSCs, and their photovoltaic (PV) performance, operational stability, and bending durability were evaluated. This thickness was chosen based on a preliminary optimization study (not presented here). The p-i-n f-PSC architecture adopted here is illustrated in Fig. 3A, and the corresponding energy-levels diagram is presented in Fig. 3B, where the MHP thin film is sandwiched between the NiO_x HTL and (6,6)-phenyl-C(61)-butyric acid methyl ester (PCBM) electron-transport layer (ETL). A thin layer of an organic salt, 4-(aminomethyl) piperidinium diiodide ((4AMP)I2), was spin-coated on the MHP thin film prior to PCBM deposition, which helps passivate the MHP top surface.³⁹ Additionally, a thin buffer layer of bathocuproine (BCP) was spin-coated on top of PCBM prior to the deposition of the top Ag electrode. The flexible substrate (~185 µm thickness) used here is indium-tin-oxide (ITO) coated polyethylene terephthalate (PET). Figure 3C plots the current density (*J*)-voltage (*V*) curves of the 'champion' FASnI₃-based and FASn_{0.9}Ge_{0.1}I₃-based f-PSCs in reverse and forward scans under AM1.5G 1sun illumination in air. The FASn_{0.9}Ge_{0.1}I₃-based f-PSC shows reduced hysteresis index (H.I.=0.043), and in reverse scan, $V_{\rm OC}$ is 0.69 V, short circuit current ($J_{\rm SC}$) is 21.3 mA·cm⁻², fill factor (FF) is 0.71, and PCE is 10.43%. This is the highest PCE reported for a Pb-free f-PSC. The $J_{\rm SC}$ value is consistent with the integrated $J_{\rm SC}$ calculated from the external quantum efficiency (EQE) spectrum in Fig. S7 in the SI. As shown in Fig. 3D, a steady PCE output of 10.3% is obtained at the MPP, which compares favorably with the extracted PCE from the J-V response, attesting to the reduced hysteresis. The evaluation of PCE of 30 FASn_{0.9}Ge_{0.1}I₃-based f-PSC

devices shows good reproducibility with an average PCE of 9.7±0.43% (Fig. 3E). The 'champion' FASnI₃-based f-PSC device has a PCE of 5.58% in reverse *J-V* scan, where *V*_{OC} is 0.53 V, *J*_{SC} is 19.2 mA·cm⁻², and FF is 0.55. The H.I. is quite high (0.148), and the average PCE measured of 30 FASnI₃-based f-PSC devices is 4.62±0.83% (Fig. 3E). In order to exclude the Ge²⁺ alloying effect, we also fabricated FASn_{0.9}Ge_{0.1}I₃-based f-PSCs, but with PEDOT:PSS HTL, instead of NiO_x. In this case, there is no interfacial GeO₂ native oxide, which is confirmed in Fig. S6 in the SI; the 'champion' f-PSC device has a PCE of 8.50% in reverse *J-V* scan, with *V*_{OC} of 0.65 V, *J*_{SC} of 20.8 mA·cm⁻², and FF of 0.63 (Fig. S8 in the SI). These PV results clearly demonstrate the beneficial effect of the interfacial GeO₂ native oxide in improving the PV performance of FASn_{0.9}Ge_{0.1}I₃-based f-PSCs with NiO_x HTL, in particular *V*_{OC} and FF.

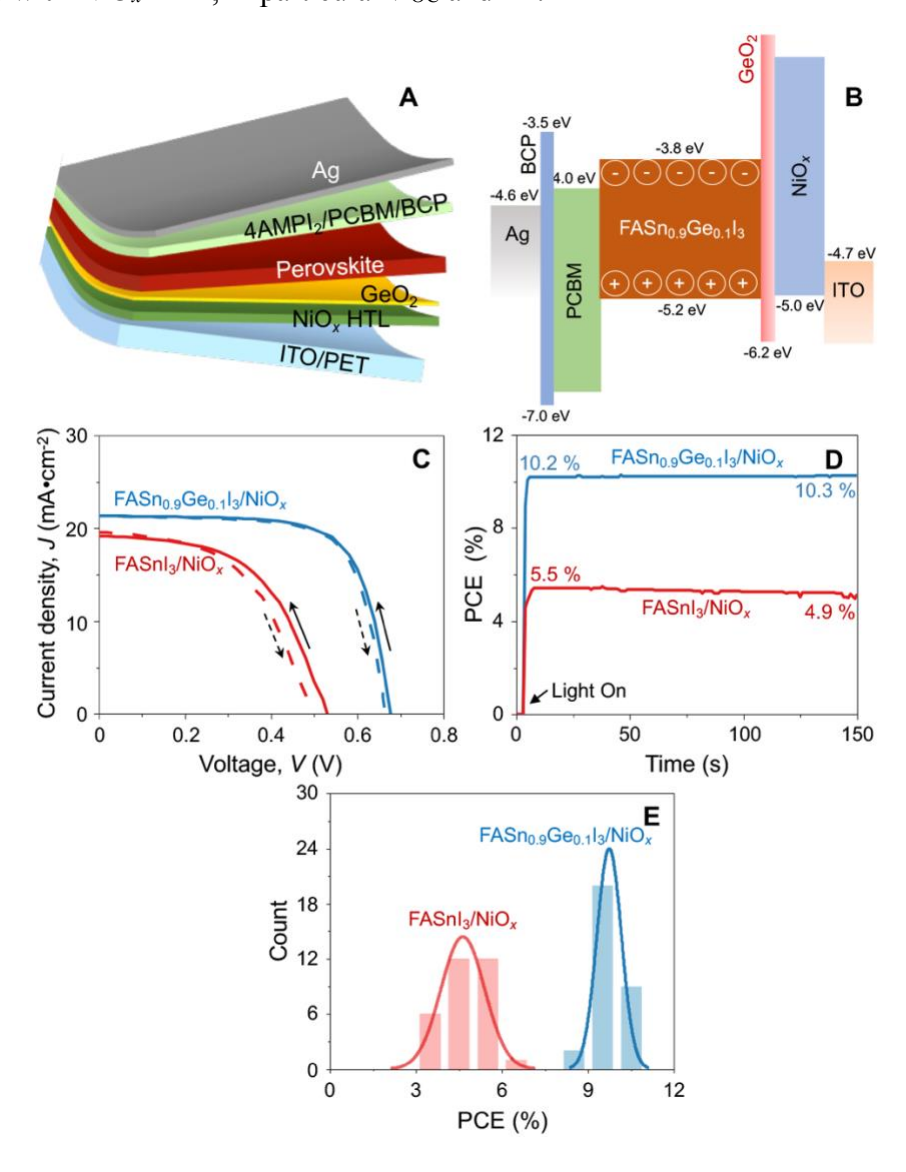


Figure 3. PV performance of FASnI₃-based and FASn_{0.9}Ge_{0.1}I₃-based f-PSCs. (A) Schematic illustration (exploded view) of the *p-i-n* f-PSC architecture (not to scale). (B) Corresponding energy-levels diagram. (C) *J-V* responses of 'champion' f-PSC devices. (D) Stable output of 'champion' f-PSC devices. (E) PCE statistics of 30 f-PSCs devices each (histogram) and probability distribution (curve).

To understand better the effect of the interfacial GeO₂ native oxide on the junction quality in these PSCs, we employed Kelvin probe force microscopy (KPFM) to characterize the crosssections of FASnI₃-based and FASn_{0.9}Ge_{0.1}I₃-based PSCs. (Note that rigid PSCs on ITO/glass substrates were used here for the convenience of obtaining clean cross-sections by cleaving.) By applying small bias voltages to the devices during the measurement, KPFM spatially resolves the voltage drop across the entire device stack at the nanometer length scale. 40 The local voltage drop is determined by the equivalent resistance of different layers and interfaces, 41, 42 and the junction quality can be evaluated by comparing the distribution of the voltages. Here we took potential profiles under various bias voltages (Figs. 4C and 4D) and deduced the corresponding electricfield differences across the device stack (Fig. 4E and 4F) by numerically calculating the derivative of the potential changes with respect to the 0-V condition. During the scans, because the electric current through the whole device must be even, the voltage drop and the strength of the electricfield difference across the device depend on the nature of the electric junction, and they are also determined by the competition between the HTL/MHP and the MHP/ETL interfaces. In both PSCs, we observe that the main junction is located at the MHP/ETL interface (Figs. 4E and 4F). However, in the FASnI₃-based PSC a small peak is observed at the HTL/MHP interface (Fig. 4E), suggesting a leakage current across the whole device stack as a result of the poor interface between the NiOx HTL and the FASnI₃ thin film. The NiO_x is expected to oxidize the Sn²⁺ in the FASnI₃, creating a thin metallic layer containing Sn-vacancies at the interface, which can lead to the leakage current, and also enhanced recombination at that interface. However, in the case of the FASn_{0.9}Ge_{0.1}I₃based PSC (Fig. 4F), due to the presence of dielectric GeO₂ native oxide at the HTL/MHP interface, no apparent leakage current is observed, and the interfacial recombination sites are expected to be reduced. These results are consistent with the higher $V_{\rm OC}$ and FF observed in the FASn_{0.9}Ge_{0.1}I₃-based f-PSCs with NiO_x HTL.

The operational-stability of unencapsulated FASnI₃-based and FASn_{0.9}Ge_{0.1}I₃-based f-PSC devices with NiO_x HTL was tested under continuous 1-sun illumination with MPP-tracking (N₂ atmosphere, ~45 °C). An FASn_{0.9}Ge_{0.1}I₃-based f-PSC with PEDOT:PSS HTL was also tested.

Figure 5A shows that the PCE of FASn_{0.9}Ge_{0.1}I₃-based f-PSC has degraded to only 80% of its initial value after 700 h (T80), whereas the PCE of the FASnI₃-based f-PSC has degraded to 50% only after 123 h. With PEDOT:PSS HTL, the PCE of the corresponding FASn_{0.9}Ge_{0.1}I₃-based f-PSC degraded to 53% of its initial value after 700 h. This demonstrates the clear advantage of having the GeO₂ native oxide at the NiO_x/FASn_{0.9}Ge_{0.1}I₃ interface in enhancing the operational-stability of these f-PSC devices. (Note that the paper that reports 8.46% PCE in a Pb-free f-PSC used storage-stability tests, results from which cannot be used for comparison here.²¹)

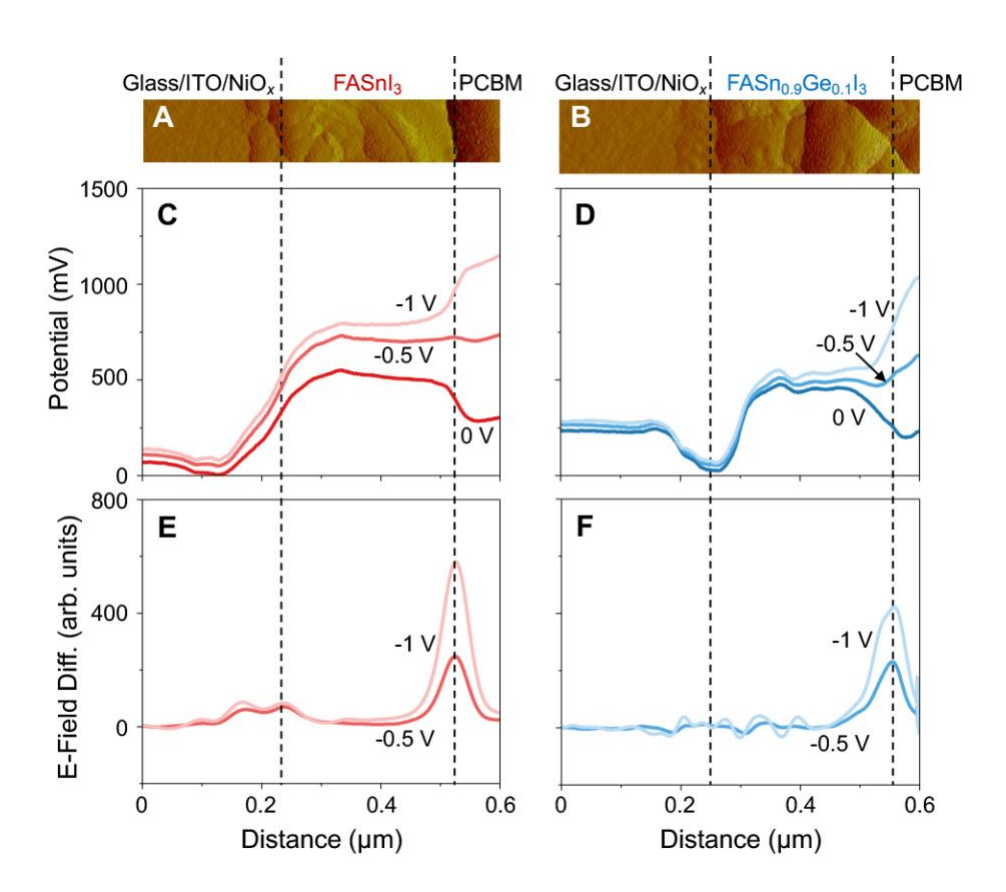


Figure 4. KPFM characterization of cross-sections of rigid PSC devices. AFM images of PSCs based on: (A) FASnI₃ and (B) FASn_{0.9}Ge_{0.1}I₃. Potential profiles recorded at 0 V, -0.5 V, and -1.0 V bias voltages of PSCs based on: (C) FASnI₃ and (D) FASn_{0.9}Ge_{0.1}I₃. Corresponding calculated electric-field-difference profiles of PSCs based on: (E) FASnI₃ and (F) FASn_{0.9}Ge_{0.1}I₃.

The mechanical reliability in terms of bending durability of unencapsulated FASnI₃-based and FASn_{0.9}Ge_{0.1}I₃-based f-PSCs with NiO_x HTL was evaluated using an automated cyclic bending test we have developed recently.⁷ An FASn_{0.9}Ge_{0.1}I₃-based f-PSC with PEDOT:PSS HTL was also tested. This test entails bending of the f-PSC draped around a mandrel of radius, *R*=5 mm,

repeatedly using a lab-built automated machine. Draping the entire PSC device around a mandrel ensures uniform uniaxial tensile stress in the active part of the f-PSC.⁴³ Here, tension-only cycles were used, where one full cycle entails flat—convex—flat sequence, with top surface being in uniform tension when convex. (Typically, one full bending cycle may entail flat—convex—flat—concave—flat sequence, but this may result in partial crack-healing during the concave (compression) part of the cycle. 43 Thus, the use of tension-only cyclic bending avoids this undesirable complication.) All experiments were conducted at 1 cycle·s⁻¹ frequency, in a N₂filled glovebox at 25 °C to preclude any environmental effects. The test was interrupted periodically, and the J-V response of the f-PSC was measured in air. The total time needed for a 2,500-cycles test was ~45 min. Figures 5B-5E present the PV parameters as a function of number of tension-only bending cycles, n. The FASn_{0.9}Ge_{0.1}I₃-based f-PSC with NiO_x HTL shows remarkable bending-durability, where 80% of the initial PCE is retained after 2,500 cycles (n80). In comparison, the FASnI₃-based f-PSC retains only 4.5% of its initial PCE, and the FASn-0.9Ge0.1I3-based f-PSC with PEDOT:PSS HTL retains 46% of its initial PCE after 2,500 cycles. It is worth noting that the loss in the PCE in the latter two f-PSCs is primarily the result of the rapid loss in their J_{SC} and V_{OC}. In contrast, all three PV parameters in the FASn_{0.9}Ge_{0.1}I₃-based f-PSC with NiO_x HTL show gradual degradation, which is attributed to the presence of the interfacial GeO₂ native oxide in that PSC. (Note that Rao, et al.²¹ have conducted a different cyclic bending test on their Pb-free f-PSCs, showing 10% reduction in the PCE after 1,000 cycles.)

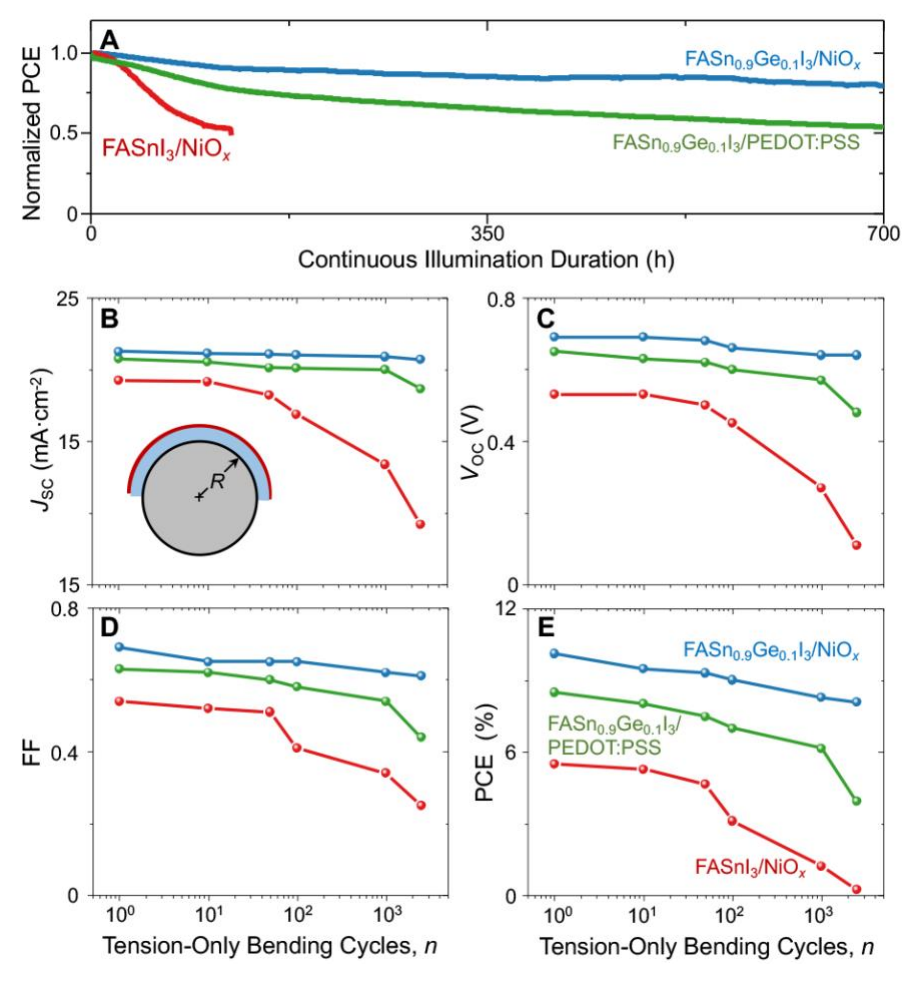


Figure 5. Operational stability and bending durability of f-PSC devices. (a) Normalized PCE of unencapsulated FASnI₃-based and FASn_{0.9}Ge_{0.1}I₃-based f-PSCs, with NiO_xHTL, and FASn_{0.9}Ge_{0.1}I₃-based f-PSC with PEDOT:PSS HTL, as a function of time under the following conditions: 1-sun continuous illumination, MPP-tracking, N₂ atmosphere, and ~45 °C. PV parameters, (b) J_{SC} , (c) V_{OC} , (d) FF, and (e) PCE, of unencapsulated FASnI₃-based and FASn_{0.9}Ge_{0.1}I₃-based f-PSCs, with NiO_x HTL, and FASn_{0.9}Ge_{0.1}I₃-based f-PSC with PEDOT:PSS HTL, as a function of number of bending cycles (*n*) under the following conditions: bending radius *R*=5 mm, tension-only cycles, 1 cycle·s⁻¹, N₂ atmosphere, and ~25 °C. Inset in (B): Inset: schematic illustration of the bending of the PSC device around a mandrel of radius *R* (not to scale).

We have demonstrated that the use of FASn_{0.9}Ge_{0.1}I₃ thin films, in conjunction with the NiO_x HTL, in f-PSCs results in the *in situ* formation of a thin (\sim 3 nm) amorphous GeO₂ native oxide at the NiO_x/FASn_{0.9}Ge_{0.1}I₃ interface. This results in several desirable effects. First, the Sn²⁺ oxidation state in the MHP is better stabilized, thereby reducing the concentration of Sn-vacancies, and the attendant reduction in both the metallic conductivity and the concentration of

recombination sites at that interface. This results in significantly improved PCE in f-PSCs (Fig. 3), over the Ge-free control f-PSCs (FASnI₃-based, with NiO_x HTL) and the NiO_x-free control f-PSCs (FASn_{0.9}Ge_{0.1}I₃-based, with PEDOT:PSS HTL). Second, the passivating interfacial GeO₂ native oxide protects the FASn_{0.9}Ge_{0.1}I₃ thin film, which manifests as significantly improved operational-stability over the control f-PSCs (Fig. 5A). Third, the interfacial GeO₂ native oxide is expected to promote enhanced mechanical bonding between the FASn_{0.9}Ge_{0.1}I₃ thin film and the NiO_x HTL. This appears to be responsible for reduced delamination cracking of that critical interface under repeated bending of the f-PSCs to a relatively sharp radius (*R*=5 mm), and retention of the PV function (Fig. 5E).

In this context, the uniaxial applied tensile stress, σ_A , in the MHP thin film due to the convex bending around a cylinder of radius R can be estimated using:⁴⁴

$$\sigma_{A} = \frac{Eh}{2R}, \tag{1}$$

where E is the Young's modulus of the MHP, and h is the total thickness of the f-PSC. The E of FASnI₃ has been estimated at 8.2 GPa,⁴⁵ assuming a Poisson's ratio (v) of 0.33. (E of FASn-0.9Ge0.1I₃ MHP has not been measured, therefore, the FASnI₃ value is used here.) Since $h\sim185$ µm, the σ_A is estimated at ~150 MPa. Additionally, the as-processed MHP thin film is typically under equi-biaxial residual tension (σ_R) due to the coefficient of thermal expansion (CTE) mismatch with the substrate, which is given by:⁴⁴

$$\sigma_{\rm R} = \frac{E(\alpha_{\rm MHP} - \alpha_{\rm ITO/PET})\Delta T}{1 - \nu},\tag{2}$$

where the CTE α_{MHP} for FASnI₃ is ~37×10⁻⁶ °C⁻¹ ⁴⁶ and that for the substrate $\alpha_{ITO/PET}$ is ~12×10⁻⁶ °C⁻¹,⁴⁷ and the temperature range through which the MHP thin film is cooled is ΔT =77 °C (100-23 °C). (The CTE of FASn_{0.9}Ge_{0.1}I₃ MHP has not been measured, therefore, the FASnI₃ value is used here.) Thus, σ_R is estimated at a modest ~24 MPa, which augments the applied uniaxial tensile stress, σ_A . The combined stresses are sufficient for the MHP film to crack (channel-cracking normal to the interface) considering the highly brittle nature of halide MHPs.⁴⁸ While such cracking by itself is unlikely to affect the PV performance significantly, it provides new free surfaces (edges) for the more dangerous interfacial delamination cracking to occur.^{7, 43, 49} The driving force, or the steady-state strain-energy release rate (*G*), for such interfacial cracking is given by:⁵⁰

$$G = \frac{(1-\nu^2)t\sigma_{\rm T}^2}{2E} , \qquad (3)$$

where t (~300 nm) is the thickness of the MHP thin film, σ_T =(σ_A + σ_R), and $G \ge G_C$ is the delamination cracking criterion, with G_C being the steady-state interfacial toughness. Using Eqn. 3, the G is estimated at ~0.5 J·m⁻². While this G estimate is relatively small, it is greater than the G_C of some of the more brittle, poorly-bonded interfaces found in PSCs (as low as 0.12 J·m⁻² ⁵¹). The G_C values of the various interfaces in the PSCs studied here have not been measured, but it is likely that G_C of the NiO_x/FASnI₃ interface is similarly low. This is deemed responsible for the rapid decrease in the PCE of FASnI₃-based f-PSCs as the interfacial cracking damage accumulates with each bending cycle (Fig. 5E). The vastly superior bending-durability of FASn_{0.9}Ge_{0.1}I₃-based f-PSCs (Fig. 5E) suggests that *in situ* formation of the GeO₂ native oxide effectively toughens the critical NiO_x/FASn_{0.9}Ge_{0.1}I₃ interface. It is well known that an *in-situ* grown interfacial layer between thin film and substrate (reaction-bonding), tends to promote mechanical bonding. ⁵⁰ The net result is the enhanced mechanical reliability of FASn_{0.9}Ge_{0.1}I₃-based f-PSCs.

In closing, f-PSCs offer some unique advantages for consumer applications, and it is desirable to remove toxic Pb from f-PSCs for better commercial prospects. Innovative approaches involving compositional and interfacial engineering, like the ones presented here, to enhance all three performance metrics — efficiency, operational-stability, and mechanical reliability — provide a path forward for Pb-free f-PSCs to reach their full potential.

ASSOCIATED CONTENT

Supporting Information

Experimental methods, including thin-films synthesis, characterization, device fabrication, and testing; four supplementary references; and eight supplementary figures. This material is available free of charge *via* the internet at http://pubs.acs.org.

AUTHOR INFORMATION

Corresponding Authors

Min Chen — School of Engineering, Brown University, Providence, Rhode Island, 02912, United States; National Renewable Energy Laboratory, Golden, CO, 80401, United States; Email: min chen1@alumni.brown.edu (M.C.)

Nitin P. Padture — School of Engineering, Brown University, Providence, Rhode Island, 02912, United States; Email: nitin_padture@brown.edu (N.P.P.)

Authors

Qingshun Dong — State Key Laboratory of Fine Chemicals, Department of Chemistry, School of Chemical Engineering, Dalian University of Technology, Dalian, 116024, China

Chuanxiao Xiao — National Renewable Energy Laboratory, Golden, CO, 80401, United States

Xiaopeng Zheng — National Renewable Energy Laboratory, Golden, CO, 80401, United States

Zhenghong Dai — School of Engineering, Brown University, Providence, Rhode Island, 02912, United States

Yantao Shi — State Key Laboratory of Fine Chemicals, Department of Chemistry, School of Chemical Engineering, Dalian University of Technology, Dalian, 116024, China

Joseph M. Luther — National Renewable Energy Laboratory, Golden, CO, 80401, United States

Author Contributions

M.C., Q.D. and C.X. contributed equally. M.C. and N.P.P. conceived the idea together, designed most of the experiments, and coordinated the project. M.C. and Q.D. prepared the MHP films, fabricated the devices, and performed most of the characterization and testing experiments. C.X., X.Z., and Z.D. performed some of the characterization and testing experiments, and the associated analyses. Y.S. and J.M.L. analyzed some of the results. M.C. and N.P.P. co-wrote the manuscript, with input from all the other authors.

Notes

The authors declare no competing financial interest.

ACKNOWLEDGEMENTS

The work at Brown University was supported by the National Science Foundation (grant nos. OIA-1538893 and DMR-2102210) and the Office of Naval Research (grant no. N00014-20-1-2574). This work was also authored in part by the National Renewable Energy Laboratory (NREL), operated by Alliance for Sustainable Energy, LLC, for the U.S. Department of Energy (DOE) under contract No. DE-AC36-08GO28308. Funding to NREL was provided U.S. Department of Energy Office of Energy Efficiency and Renewable Energy Solar Energy

Technologies Office under the De-Risking Perovskites Program. The views expressed in the article do not necessarily represent the views of the DOE or the U.S. Government. The work at Dalian University of Technology was supported by the National Natural Science Foundation of China (grant no. 22005043). We thank Dr. Chao Zhu of Nanyang Technological University, Singapore for performing the TEM characterization.

REFERENCES

- 1. Kojima, A.; Teshima, K.; Shirai, Y.; Miyasaka, T., Organometal Halid Perovskites as Visible-Light Sensitizers for Photovoltaic Cells. *J. Am. Chem. Soc.* **2009**, *131*, 6050-6051.
- 2. Miyasaka, T., Perovskite Photovoltaics and Optoelectronics: From Fundamentals to Advanced Applications. Wiley-VCH: Weinheim, Germany, 2021.
- 3. NREL, <u>https://www.nrel.gov/pv/cell-efficiency.html</u> (accessed on March 30, 2022).
- 4. Jung, H. S.; Han, G. S.; Park, N.-G.; Ko, M. J., Flexible Perovskite Solar Cells. *Joule* **2019**, *3*, 1850-1880.
- 5. Zhang, J.; Zhang, W.; Cheng, H.-M.; Silva, S. R. P., Critical review of recent progress of flexible perovskite solar cells. *Mater. Today* **2020**, *39*, 66-88.
- 6. Tang, G.; Yan, F., Recent Progress of Flexible Perovskite Solar Cells. *Nano Today* **2021,** *39*, 101155.
- 7. Dong, Q.; Chen, M.; Liu, Y.; Eickemeyer, F. T.; Zhao, W.; Dai, Z.; Yin, Y.; Jiang, C.; Feng, J.; Jin, S.; Liu, S.; Zakeeruddin, S. M.; Grätzel, M.; Padture, N. P.; Shi, Y., Flexible Perovskite Solar Cells with Simultaneously Improved Efficiency, Operational Stability, and Mechanical Reliability. *Joule* **2021**, *5*, 1587-1601.
- 8. Ju, M.-G.; Chen, M.; Zhou, Y.; Dai, J.; Ma, L.; Padture, N. P.; Zeng, X. C., Towards Ecofriendly and Stable Perovskite Materials for Photovoltaics. *Joule* **2018**, *2*, 1231-1241.
- Moody, N.; Sesena, S.; deQuilettes, D. W.; Dou, B. D.; Swartwout, R.; T.Buchman, J.; Johnson, A.; Eze, U.; Brenes, R.; Johnston, M.; L.Haynes, C.; Bulović, V.; G.Bawendi, M., Assessing the Regulatory Requirements of Lead-Based Perovskite Photovoltaics. *Joule* 2020, 4, 970-974.
- 10. Ke, W.; Kanatzidis, M. G., Prospects for Low-Toxicity Lead-Free Perovskite Solar Cells. *Nature Commun.* **2019**, *10*, 965.

- 11. Du, K.; Meng, W.; Wang, X.; Yan, Y.; Mitzi, D. B., Bandgap Engineering of Lead-Free Double Perovskite Cs₂AgBiBr₆ through Trivalent Metal Alloying. *Angew. Chem. Intl. Ed.* **2017**, *56*, 8158-8162.
- 12. Zhang, Z.; Li, X.; Xia, X.; Wang, Z.; Huang, Z.; Lei, B.; Gao, Y., High-Quality (CH₃NH₃)₃Bi₂I₉ Film-Based Solar Cells: Pushing Efficiency up to 1.64%. *J. Phys. Chem. Lett.* **2017**, *8*, 4300-4307.
- 13. Zuo, C.; Ding, L., Lead-Free Perovskite Materials (NH₄)₃Sb₂I_xBr_{9-x}. *Angew. Chem. Intl. Ed.* **2017,** *56*, 6528-6532.
- 14. Chen, M.; Ju, M.-G.; Carl, A. D.; Zong, Y.; Grimm, R. L.; Gu, J.; Zeng, X. C.; Zhou, Y.; Padture, N. P., Stable Perovskite Solar Cells Based on Cesium Titanium (IV) Bromide Double Perovskite Thin Films. *Joule* **2018**, *2*, 558-570.
- 15. Ju, M.-G.; Chen, M.; Zhou, Y.; Garces, H. F.; Dai, J.; Ma, L.; Padture, N. P.; Zeng, X. C., Earth-Abundant Non-Toxic Titanium (IV) Based Vacancy-Ordered Double Perovskite Halides with Tunable 1.0 to 1.8 eV Bandgaps for Photovoltaic Applications. *ACS Energy Lett.* **2018**, *3*, 297-304.
- Krishnamoorthy, T.; Ding, H.; Yan, C.; Leong, W. L.; Baikie, T.; Zhang, Z.; Sherburne,
 M.; Li, S.; Asta, M.; Mathews, N.; Mhaisalkar, S. G., Lead-Free Germanium Iodide
 Perovskite Materials for Photovoltaic Applications. J. Mater. Chem. A 2015, 3, 23829-23832.
- 17. Hao, F.; Stoumpos, C. C.; Cao, D. H.; Chang, R. P. H.; Kanatzidis, M. G., Lead-Free Solid-State Organic-Inorganic Halide Perovskite Solar Cells. *Nature Photon.* **2014**, *8*, 489-494.
- 18. Wu, T.; Liu, X.; Luo, X.; Lin, X.; Cui, D.; Wang, Y.; Segawa, H.; Zhang, Y.; Han, L., Lead-free tin perovskite solar cells. *Joule* **2021**, *5*, 863-886.
- Chen, M.; Ju, M.-G.; Garces, H. F.; Carl, A. D.; Ono, L. K.; Hawash, Z.; Zhang, Y.; Shen, T.; Qi, Y.; Grimm, R. L.; Pacifici, D.; Zeng, X. C.; Zhou, Y.; Padture, N. P., Highly Stable and Efficient All-Inorganic Lead-Free Perovskite Solar Cells with Native-Oxide Passivation. *Nature Commun.* 2019, 10, 16.
- Zhou, J.; Hao, M.; Zhang, Y.; Ma, X.; Dong, J.; Lu, F.; Wang, J.; Wang, N.; Zhou, Y., Chemo-Thermal Surface Dedoping for High Performance Tin Perovskite Solar Cells. *Matter* 2022, 5, 683-693.
- Rao, L.; Meng, X.; Xiao, S.; Xing, Z.; Fu, Q.; Wang, H.; Gong, C.; Hu, T.; Hu, X.; Guo, R.; Chen, Y., Wearable Tin-Based Perovskite Solar Cells Achieved by a Crystallographic Size Effect. *Angew. Chem. Intl. Ed.* 2021, 60, 14693-14700.

- 22. Li, W.; Li, J.; Fan, J.; Mai, Y.; Wang, L., Addictive-Assisted Construction of All-Inorganic CsSnIBr₂ Mesoscopic Perovskite Solar Cells with Superior Thermal Stability up to 473 K. *J. Mater. Chem. A* **2016**, *4*, 17104-17110.
- 23. Mitzi, D. B.; Wang, S.; Field, C. A.; Chess, C. A.; Guloy, A. M., Conducting Layered Organic-inorganic Halides Containing <110>-Oriented Perovskite Sheets. *Science* **1995**, *267*, 1473-1476.
- 24. Li, B.; Chang, B.; Pan, L.; Li, Z.; Fu, L.; He, Z.; Yin, L., Tin-Based Defects and Passivation Strategies in Tin-Related Perovskite Solar Cells. *ACS Energy Lett.* **2020,** *5*, 3752-3772.
- 25. Noel, N. K.; Stranks, S. D.; Abate, A.; Wehrenfenning, C.; Guarnera, S.; Haghighirad, A.; Sadhanal, A.; Eperon, G. E.; Pathak, S. K.; Johnston, M. B.; Petrozza, A.; Herz, L. M.; Snaith, H. J., Lead-Free Organic-Inorganic Tin Halide Perovskites for Photovoltaic Applications. *Energy Environ. Sci.* 2014, 7, 3061-3068.
- 26. Chung, I.; Lee, B.; He, J.; Chang, R. P. H.; Kanatzidis, M., All-Solid-State Dye-Sensitized Solar Cells with High Efficiency. *Nature* **2012**, *485*, 486-490.
- 27. Song, T.-B.; Yokoyama, T.; Aramaki, S.; Kanatzidis, M. G., Performance Enhancement of Lead-Free Tin-Based Perovskite Solar Cells with Reducing Atmosphere-Assisted Dispersible Additive. *ACS Energy Lett.* **2017**, *2*, 897-903.
- 28. Jiang, X.; Li, H.; Zhou, Q.; Wei, Q.; Wei, M.; Jiang, L.; Wang, Z.; Peng, Z.; Wang, F.; Zang, Z.; Xu, K.; Hou, Y.; Teale, S.; Zhou, W.; Si, R.; Gao, X.; Sargent, E. H.; Ning, Z., One-Step Synthesis of SnI₂·(DMSO)_x Adducts for High-Performance Tin Perovskite Solar Cells. *J. Am. Chem. Soc.* **2021**, *143*, 10970-10976.
- 29. Wang, F.; Jiang, X.; Chen, H.; Shang, Y.; Liu, H.; Wei, J.; Zhou, W.; He, H.; Liu, W.; Ning, Z., 2D-Quasi-2D-3D Hierarchy Structure for Tin Perovskite Solar Cells with Enhanced Efficiency and Stability. *Joule* **2018**, *2*, 2732-2743.
- 30. Shao, S.; Nijenhuis, M.; Dong, J.; Kahmann, S.; Brink, G. H. t.; Portale, G.; Loi, M. A., Influence of the stoichiometry of tin-based 2D/3D perovskite active layers on solar cell performance. *J. Mater. Chem. A* **2021**, *9*, 10095-10103.
- 31. Nishimura, K.; Kamarudin, M. A.; Hirotani, D.; Shen, Q.; Minemoto, T.; Yoshino, K.; Hayase, S., Pb-Free Sn-Perovskite Solar Cells with Over 13% Efficiency. *Proc. SPIE, Organic, Hybrid, and Perovskite Photovoltaics XXI* **2020**, 114740X.

- 32. Manders, J. R.; Tsang, S.-W.; Hartel, M. J.; Lai, T.-H.; Chen, S.; Amb, C. M.; Reynolds, J. R.; So, F., Solution-Processed Nickel Oxide Hole Transport Layers in High Efficiency Polymer Photovoltaic Cells. *Advanced Funct. Mater.* **2013**, *23*, 2993-3001.
- 33. Meng, X.; Wang, Y.; Lin, J.; Liu, X.; He, X.; Barbaud, J.; Wu, T.; Noda, T.; Yang, X.; Han, L., Surface-Controlled Oriented Growth of FASnI₃ Crystals for Efficient Lead-free Perovskite Solar Cells. *Joule* **2020**, *4*, 902-912.
- 34. Jeon, N. J.; Noh, J. H.; Kim, Y. C.; Yang, W. S.; Ryu, S.; Seok, S. I., Solvent Engineering for High-Performance Inorganic-Organic Hybrid Perovskite Solar Cells. *Nature Mater.* **2014**, *9*, 897-903.
- 35. Zhou, Y.; Game, O. S.; Pang, S.; Padture, N. P., Microstructures of Organometal Trihalide Perovskites for Solar Cells: Their Evolution from Solutions and Characterization. *J. Phys. Chem. Lett.* **2015**, *6*, 4827-4839.
- 36. Dunlop-Shohl, W. A.; Zhou, Y.; Padture, N. P.; Mitzi, D. B., Synthetic Approaches for Halide Perovskite Thin Films. *Chem. Rev.* **2019**, *119* (5), 3193-3295.
- 37. Ito, N.; Kamarudin, M. A.; Hirotani, D.; Zhang, Y.; Shen, Q.; Ogomi, Y.; Iikubo, S.; Minemoto, T.; Yoshino, K.; Hayase, S., Mixed Sn–Ge Perovskite for Enhanced Perovskite Solar Cell Performance in Air. *J. Phys. Chem. Lett.* **2018**, *9*, 1682-1688.
- 38. Wu, Y.-H; Wu, M.-L.; Lyu, R.-J.; Wu, J.-R.; Lin, C.-C.; Chen, L.-L., Comparison of Ge Surface Passivation Between SnGe_x Films Formed by Oxidation of Sn/Ge and Sn/Ge_x/Ge Structures. *IEEE Electron Device Lett.* **2011**, 32, 611-613.
- 39. Hu, M.; Chen, M.; Guo, P.; Zhou, H.; Deng, J.; Yao, Y.; Jiang, Y.; Gong, J.; Dai, Z.; Zhou, Y.; Qian, F.; Chong, X.; Feng, J.; Schaller, R. D.; Zhu, K.; Padture, N. P.; Zhou, Y., Sub-1.4 eV Bandgap Inorganic Perovskite Solar Cells with Long-Term Stability. *Nature Commun.* **2020**, *11*, 151.
- 40. Cui, P.; Wei, D.; Ji, J.; Huang, H.; Jia, E.; Dou, S.; Wang, T.; Wang, W.; Li, M., Planar *p*–*n* Homojunction Perovskite Solar Cells with Efficiency Exceeding 21.3%. *Nature Energy* **2019**, *4*, 150-159.
- 41. Xiao, C.; Wang, C.; Ke, W.; Gorman, B. P.; Ye, J.; Jiang, C.-S.; Yan, Y.; Al-Jassim, M. M., Junction Quality of SnO₂-Based Perovskite Solar Cells Investigated by Nanometer-Scale Electrical Potential Profiling. *ACS Appl. Mater. Interf.* **2017**, *9*, 38373-38380.

- 42. Xiao, C.; Zhang, F.; Chen, X.; Yang, M.; Harvey, S. P.; Beard, M. C.; Berry, J. J.; Jiang, C.-S.; Al-Jassim, M. M.; Zhu, K., SMART Perovskite Growth: Enabling a Larger Range of Process Conditions. *ACS Energy Lett.* **2021**, *6* (2), 650-658.
- 43. Yadavalli, S. K.; Dai, Z.; Zhou, H.; Zhou, Y.; Padture, N. P., Facile Crack-Healing in Organic-Inorganic Halide Perovskite Thin Films. *Acta Mater.* **2020**, *187*, 112-121.
- Rolston, N.; Bush, K. A.; Printz, A. D.; Gold-Parker, A.; Ding, Y.; Toney, M. F.; McGehee,
 M. D.; Dauskardt, R. H., Engineering Stress in Perovskite Solar Cells to Improve Stability.
 Adv. Energy Mater. 2018, 8, 1802139.
- 45. Lee, Y.; Mitzi, D. B.; Barnes, P. W.; Vogt, T., Pressure-Induced Phase Transitions and Templating Effect in Three-Dimensional Organic-Inorganic Hybrid Perovskites. *Phys. Rev. B* **2003**, *68*, 020103.
- 46. Dang, Y.; Zhou, Y.; Liu, X.; Ju, D.; Xia, S.; Xia, H.; Tao, X., Formation of Hybrid Perovskite Tin Iodide Single Crystals by Top-Seeded Solution Growth. *Angew. Chem. Intl. Ed.* **2016**, *55*, 3447-3450.
- 47. Chien, C.-H.; Chen, T.; Su, F.-I.; Lin, C.-Y.; Su, T.-H.; Lin, Y.-M.; Liu, Y.-C.; Tsay, T.-L., Thickness Effects on the Thermal Expansion Coefficient of Indium Tin Oxide/Polyethylene Terephthalate Film. *Expt.Tech.* **2016**, *40* (2), 639-644.
- 48. Ramirez, C.; Yadavalli, S. K.; Garces, H. F.; Zhou, Y.; Padture, N. P., Thermo-Mechanical Behavior of Organic-Inorganic Halide Perovskites for Solar Cells. *Scripta Mater.* **2018**, *150*, 36-41.
- 49. Dai, Z.; Yadavalli, S. K.; Chen, M.; Abbaspourtamijani, A.; Qi, Y.; Padture, N. P., Interfacial Toughening with Self-Assembled Monolayers Enhances Perovskite Solar Cells Reliability. *Science* **2021**, *372*, 618-622.
- 50. Freund, L. B.; Suresh, S., *Thin Film Materials: Stress, Defect Formation and Surface Evolution*. Cambridge University Press: Cambridge, UK, 2003.
- 51. Rolston, N.; Watson, B. L.; Bailie, C. D.; McGehee, M. D.; Bastos, J. P.; Gehlhaar, R.; Kim, J.-E.; Vak, D.; Mallajosyula, A. T.; Gupta, G.; Mohite, A. D.; Dauskardt, R. H., Mechanical Integrity of Solution-Processed Perovskite Solar Cells. *Ext. Mech. Lett.* **2016**, *9*, 353-358.